

Pore-scale dispersion: Bridging the gap between microscopic pore structure and the emerging macroscopic transport behavior

Daniel W. Meyer*

Institute of Fluid Dynamics, ETH Zürich, Sonneggstrasse 3, CH-8092 Zürich, Switzerland

Branko Bijeljic

Department of Earth Science and Engineering, Prince Consort Road, Imperial College, London SW7 2BP, United Kingdom

(Received 8 March 2016; revised manuscript received 23 May 2016; published 14 July 2016)

We devise an efficient methodology to provide a universal statistical description of advection-dominated dispersion ($Péclet \rightarrow \infty$) in natural porous media including carbonates. First, we investigate the dispersion of tracer particles by direct numerical simulation (DNS). The transverse dispersion is found to be essentially determined by the tortuosity and it approaches a Fickian limit within a dozen characteristic scales. Longitudinal dispersion was found to be Fickian in the limit for bead packs and superdiffusive for all other natural media inspected. We demonstrate that the Lagrangian velocity correlation length is a quantity that characterizes the spatial variability for transport. Finally, a statistical transport model is presented that sheds light on the connection between pore-scale characteristics and the resulting macroscopic transport behavior. Our computationally efficient model accurately reproduces the transport behavior in longitudinal direction and approaches the Fickian limit in transverse direction.

DOI: [10.1103/PhysRevE.94.013107](https://doi.org/10.1103/PhysRevE.94.013107)

I. INTRODUCTION

Flow and transport processes in natural porous media are of importance in applications such as subsurface hydrology [1], enhanced oil recovery [2], and carbon capture and storage [3]. Despite its significance, the *in situ* study of flow and transport at the pore scale is still at an early stage. Based on nuclear magnetic resonance (NMR) pore-size and particle displacement statistics have been gathered around 1990 as summarized by Sahimi [4, Section 4] and Scheven *et al.* [5], respectively. More detailed experimental investigations focusing on resolved flow fields in upscaled media, e.g., bead packs, were conducted by Moroni and Cushman [6] and Moroni *et al.* [7] at the beginning of this century. Only quite recently, corresponding microscale experiments were documented [8,9]. The more recent studies [6–9] focus on three-dimensional configurations to inspect transport or dispersion in both mean-flow parallel, i.e., longitudinal, and transverse directions. Moreover, they point out the need for devising an efficient macroscopic representation of the microscopic pore-scale dynamics, which is the main goal of our work.

Of particular interest in the context of subsurface transport is the transition from an initially ballistic dispersion regime, where the particle displacement variance grows quadratically with time, to an asymptotic Fickian regime with linear growth. The particle displacement variance is important as it characterizes the plume spreading. Moreover, the particle travel length and time scales at which Fickian behavior is reached determine the range of applicability of Fickian dispersion models [10,11]. While in some experiments conducted by Moroni and Cushman [6] and Moroni *et al.* [7] the asymptotic regime was reached within the limited test section, preasymptotic behavior was recorded in others.

Advances in the area of micro-computerized tomography (micro-CT) made over the past decade permit the acqui-

sition of microscale pore-space geometries to extract, for example, flow and transport characteristics like the effective permeability, which is useful for Darcy-flow simulations [12,13]. Moreover, the availability of detailed pore-space geometries enables single-phase flow and transport direct numerical simulation (DNS) as documented in Refs. [14–18]. The resulting flow fields provide valuable data to study the microscopic transport process in detail. Furthermore, this data gives important guidance for the development of effective models that can be applied to simulate flow and transport at scales larger than the pore scale [19,20]. For example, Kang *et al.* [19] studied the advection-dominated dispersion in Berea sandstone based on a flow field stemming from micro-CT scanning and pore-scale DNS. They found that the dispersion in longitudinal direction is superdiffusive, with the variance of tracer particle positions scaling with time to the power of 1.5. On the other hand, subdiffusive behavior in transverse direction with an exponent of 0.8 was reported. Transverse dispersion is of particular importance as it controls biodegradation of organic contaminant plumes to name only one prominent example [21–23].

Kang *et al.* [19], as well as de Anna *et al.* [24] in a two-dimensional synthetic porous medium, showed that the Lagrangian time series of tracer particle velocities are highly asymmetric with long correlated periods at low velocities interrupted by high-velocity bursts. A very similar Lagrangian behavior was observed and successfully modeled at the Darcy scale, where highly heterogeneous two-dimensional conductivity fields lead to irregular flow fields involving flow focusing and defocusing [25–27].

In their model, Meyer *et al.* [26] applied a coupled spatiotemporal Markov process, where the irregular behavior of the velocity magnitude was accounted for by a temporal Markov process and the particle path-line geometry—which reflects the spatial conductivity distribution—was represented by a spatial velocity-direction-angle process. In this work, we apply an analogous approach at the pore scale for

*meyerda@ethz.ch

monodisperse bead packs, Bentheimer sandstone, and Ketton and Estailades carbonates with the goal of efficiently representing macroscopic transport behavior from microscopic pore-scale dynamics. Moreover, we want to rigorously test our proposed model's ability to universally describe transport in pore structures with various degrees of complexity. Unlike previous studies [19,20], we include carbonate rocks that have most complex pore structures. Carbonates are very important geological media that are estimated to hold about 60% of the world's remaining hydrocarbon resources [28]. However, before focusing on the statistical description of flow and transport at the macroscopic scale, we first document our microscale DNS-based effort in the next section.

II. PORE-SCALE DNS

The first step in our methodology is to study a range of samples with various degrees of spatial heterogeneity by means of pore-scale DNS. On the one hand, the resulting velocity statistics are used to derive a dispersion description and model applicable for all samples considered. On the other hand, the resulting transport data is used as a reference for model validation. The cubical samples used in this study have side lengths L_0 of the order of 1 mm and were scanned at voxel resolutions Δx around $3 \mu\text{m}$. Image segmentation was applied to identify solid and void voxels [16–18]. The voxel mesh of the monodisperse bead packs were determined based on sphere center measurements of Finney [29] and subsequent segmentation by Prodanovic and Bryant [30]. A characteristic average pore-length scale $L \equiv \pi V/S$ was extracted from each pore geometry based on the ratio of the total sample volume V (void and solid space) to the solid and void interface area S . For consolidated sandstones and carbonates, L provides an estimate for the grain size [31, p.1133]. A summary of sample cross sections and characteristics including the porosity ϕ is provided in Table I. The bead diameter $d = 100 \mu\text{m}$ for the 300 and 500 bead packs were set such that $L_0/d = 6$ and 10, respectively. It is pointed out that for most samples L_0/L is around 10 or higher. We clarify that samples of the same media type represent different pore-space geometries and are not the result of scans of the same geometry with different resolutions.

Flow was induced in the pore space by applying a unit pressure drop of 1 Pa over the in- and outflow planes located at positions $x_1 = 0$ and L_0 , respectively, of the sample cube. With no-flow boundary conditions applied at all other planes, this leads to a mean flow in x_1 -direction of the 3D pore space $\mathbf{x} = (x_1, x_2, x_3)^T$. More details about the numerical calculation of the flow field $\mathbf{u} = (u_1, u_2, u_3)^T$ are provided in Ref. [17, Section 2.3]. We point out that the pore-space geometries, that are characterized by ϕ and that are used for the flow computations, are composed exclusively of all void voxels that are connected to both the in- and outflow planes. To normalize the flow field, the mean velocity at the inflow plane defined as $U \equiv \int_0^{L_0} \int_0^{L_0} u_1(0, x_2, x_3) dx_2 dx_3 / (L_0^2 \phi)$ was used. For a statistically space-stationary and sufficiently large sample, U approximates the mean displacement velocity of tracer particles in the x_1 direction. Lagrangian path lines are characterized in Table I through the tortuosity κ being the ratio of the length of the unwrapped tortuous particle path and the travel distance in the mean flow direction.

To study transport in the listed samples, particles were released at uniformly distributed random locations in pore space and tracked with the semianalytical, mass-conservative scheme of Pollock [32]. To emulate a virtually infinite porous medium but at the same time recover Lagrangian velocity time series that are continuous over sample boundaries, the following algorithm was used to reinject particles at the inflow plane that have reached the outflow plane. The exit velocity of a particle sitting at the outflow plane $\mathbf{u}^{(o)}$ and all velocity vectors of voxels at the inflow plane $\mathbf{u}^{(i)}$ are expressed in cylindrical coordinates, i.e., $\mathbf{u} = (u_1, u_2, u_3)^T \rightarrow \mathbf{u}_c = (u_1, u_r, \psi)^T$ with $u_r \equiv \sqrt{u_2^2 + u_3^2}$ and $\psi \equiv \arctan(u_3/u_2)$. Next, the inflow cell is identified with component vector $(u_1, u_r)^T$ being closest to the corresponding particle vector, i.e., where the distance between $(u_1^{(o)}, u_r^{(o)})^T$ and $(u_1^{(i)}, u_r^{(i)})^T$ is smallest. Subsequent particle tracking continues from the identified inflow cell, but with the sample rotated around the x_1 direction by the difference in the ψ angles of the identified inflow cell and the particle exit velocity, i.e., $\psi^{(o)} - \psi^{(i)}$. In the case where the component vectors match, meaning that $(u_1^{(o)}, u_r^{(o)})^T = (u_1^{(i)}, u_r^{(i)})^T$, the particle velocity remains unchanged after reinjection. Sample rotation is reasonable for samples that are

TABLE I. Characteristics of the samples considered. Sample cross-sections $L_0 \times L_0$ are provided with the velocity magnitude in the void space given by the dark blue shading. All samples are in 3d with the image size consisting of n^3 voxels.

Samples	Bead pack 300	Bead pack 500	Ketton	Bentheimer 500	Bentheimer 1000	Estailades
L_0 [mm]	0.6	1	2.7	1.5	3	3.31
Δx [μm]	2	2	7.7	3	3	3.31
n	300	500	350	500	1000	1000
L_0/L	10.7	17.8	8.53	11.2	22.6	11.7
ϕ [%]	35.9	36.2	14.9	21.1	21.6	10.9
κ	1.26	1.27	1.4	1.54	1.65	2.26
λ/L	4.37	3.89	5.53	8.33	8.32	36.2

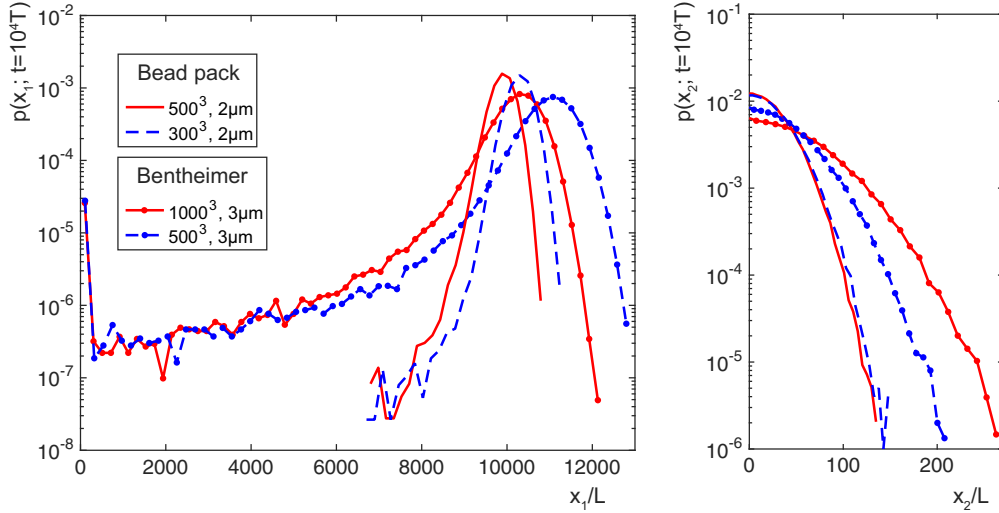


FIG. 1. Convergence of particle plumes in terms of sample size. Depicted are (left) longitudinal and (right) transverse particle position histograms after nondimensional time $t/T = 10^4$.

statistically isotropic. To normalize travel distances and times, the reference length L and time $T \equiv L/U$ were used.

Plumes that result from tracking of the order of 200 000 particles in the bead pack and Bentheimer sandstone samples of different nondimensional sizes L_0/L are depicted in Fig. 1. Besides deviations resulting from inaccuracies in the estimation of the mean plume displacement velocity (U is estimated based on samples of limited sizes), the longitudinal plumes corresponding to different sample sizes match quite well. While the plumes in the sandstone samples are relatively long and involve a peak at $x_1 \approx 0$, the bead-pack plumes are quite compact and no peak is present. In sandstone, this behavior is not resulting from isolated pores since all void pores in the simulation are connected to the in- and outflow. It is rather a reflection of the very heterogeneous flow fields involving both stagnant and high-velocity flow zones. In transverse direction, the plumes in the bead packs show close agreement. Accordingly, the transverse spreading is independent of the sample size and not prone to boundary effects. This is, however, not the case for the sandstone samples, where the larger sample involves more spreading in transverse direction. The pore-space building blocks in the bead pack, that is the beads, are equal, and accordingly the pore-space geometry involves less spatial variability (see Table I). For natural media like sandstone, the grains themselves are highly variable and accordingly the pore space is less connected and geometrically more heterogeneous. As a result, larger sandstone samples are required to obtain dispersion results that are not subject to transverse boundary effects and that are size independent. Similarly, for the very heterogeneous poorly connected Estailades carbonate convergence in terms of sample size could not be observed when comparing with a smaller sample. It is pointed out that to assess independence with respect to sample size, the characteristic length L is not a reliable indicator, since in both bead packs and sandstone samples of the order of $20L$ were used with different outcome. A quantity that better measures the scale of spatial variability for transport is the Lagrangian velocity correlation length λ introduced in the next section.

In the top half of Fig. 2, the particle position variances resulting from our DNS study are depicted and longitudinal particle plumes are shown in Figs. 3–6. In longitudinal direction, the bead pack converges after 10^4 nondimensional time units from an initially ballistic dispersion regime to a diffusive Fickian regime. This is in line with the study of Moroni *et al.* [7]. All other natural media show superdiffusive behavior. Noteworthy is the similarity between the longitudinal spreading of Ketton and Bentheimer, which have quite different grain geometries but a similar connectivity structure (see cross-sections of Ketton and Bentheimer 500 in Table I). The departure from Fickian dispersion is strongest for Estailades, which displays the most heterogeneous flow field. The superdiffusive spreading is caused by particles that are trapped in stagnant flow zones and that are only gradually mobilized (see Fig. 6). This element of plume elongation in the mean-flow direction is absent in transverse direction, where transitions from ballistic to Fickian are observed in contrast to Ref. [19] within of the order of 10 time units. A measure for the magnitude of transverse dispersion seems to be the tortuosity listed in Table I. In terms of transverse spreading and tortuosity, the samples are consistently ranked as follows: Bead packs (smallest), Ketton, Bentheimer, Estailades (largest).

III. STATISTICAL DESCRIPTION

To describe the tortuous motion of tracer particles, we use a coordinate system that is aligned with the mean flow in x_1 direction and the current particle velocity $\mathbf{u}(t)$ at time t [see Fig. 7(a)]. By tracking one single particle by means of the previously outlined algorithm over thousands of differently rotated sample copies (see third paragraph of Sec. II), we are able to extract converged Lagrangian statistics such as velocity PDFs or autocorrelation functions. Due to several common features of these statistics among the different samples, a universal statistical description or model can be formulated that is able to reproduce the previously discussed Fickian behavior and departures thereof.

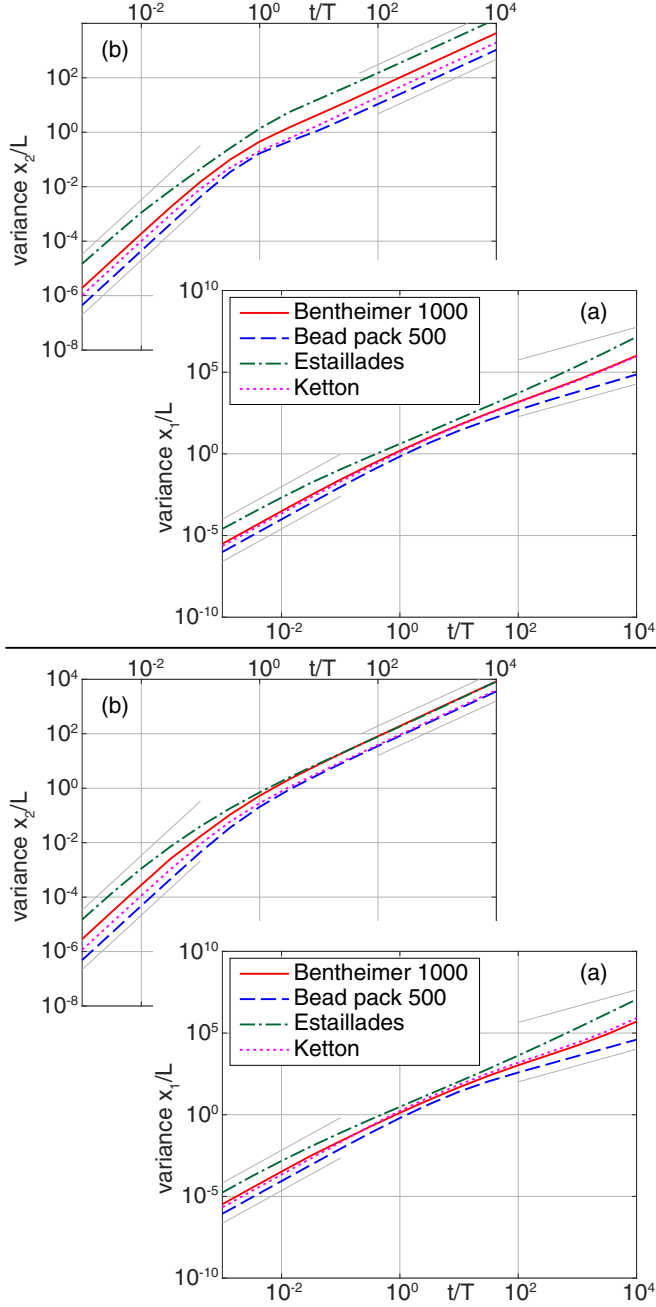


FIG. 2. Spreading of particle plumes in (top half) the DNS and (bottom half) the model computations. Depicted are the particle position variances in (a) longitudinal x_1 and (b) transverse x_2 direction, respectively. The thin straight lines at the left and right ends of the curves correspond to quadratic and linear scalings with t , respectively. Superdiffusive spreading exceeds the linear scaling.

A. Velocity process

Like in our earlier work on transport in heterogeneous conductivity fields [27], we found highly skewed PDFs of the statistically time-stationary process $u(t) \equiv |\mathbf{u}(t)|$ for all samples (not shown). To quantify the degree of correlation in $u(t)$ based on its autocorrelation function,

$$\rho_u(t) \equiv \frac{\langle [u(t_0) - \langle u \rangle][u(t_0 + t) - \langle u \rangle] \rangle}{\langle (u - \langle u \rangle)^2 \rangle},$$

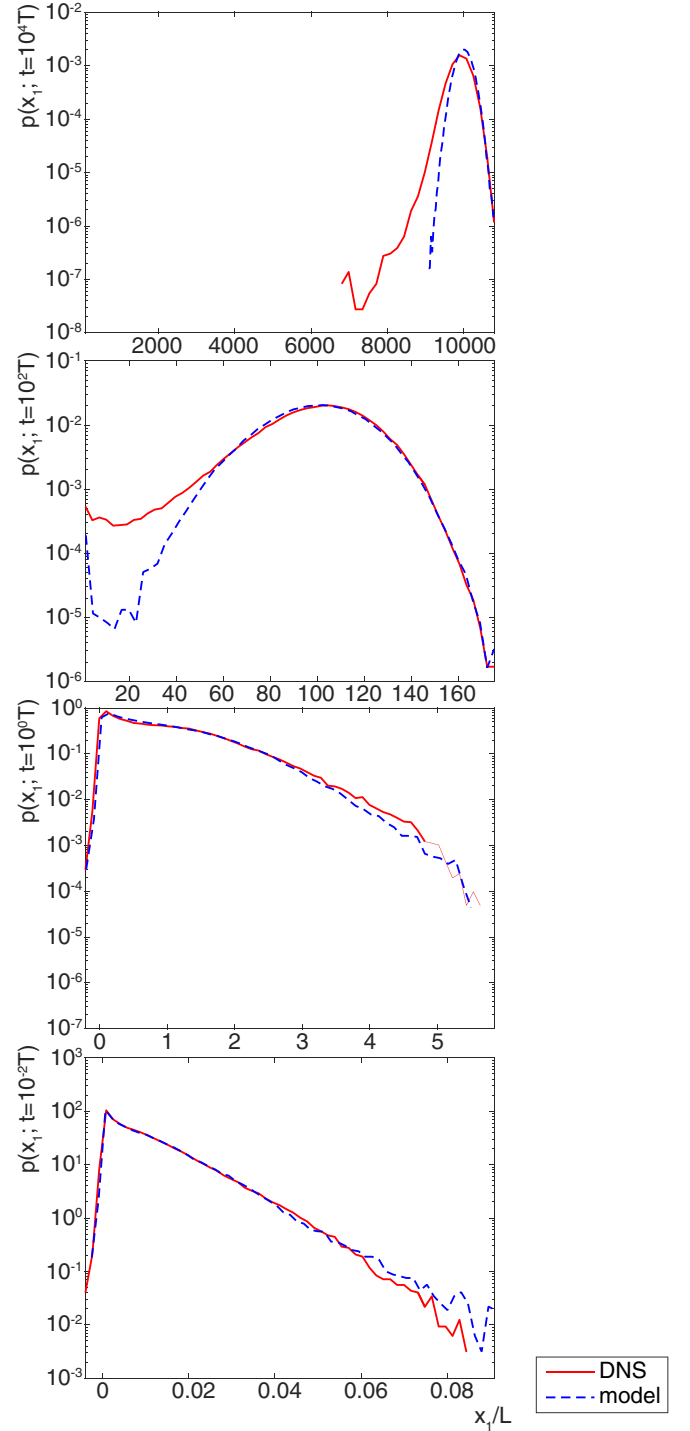


FIG. 3. Comparison of longitudinal particle plumes resulting from (solid red) DNS and (dashed blue) the statistical model. Plotted are different snapshot times. Data corresponding to the bead pack 500 sample are depicted.

we have estimated the integral timescale $\tau \equiv \int_0^\infty \rho_u(t) dt$ and list in Table I the corresponding integral length scale $\lambda \equiv U\tau$. For Estailades, λ/L is highest, which is a result of the long correlated low-velocity stretches in $u(t)$, which are visible in Fig. 8. In the bead packs, the velocity PDF is less skewed and λ is shorter. The skewness in $u(t)$ can be reduced by taking

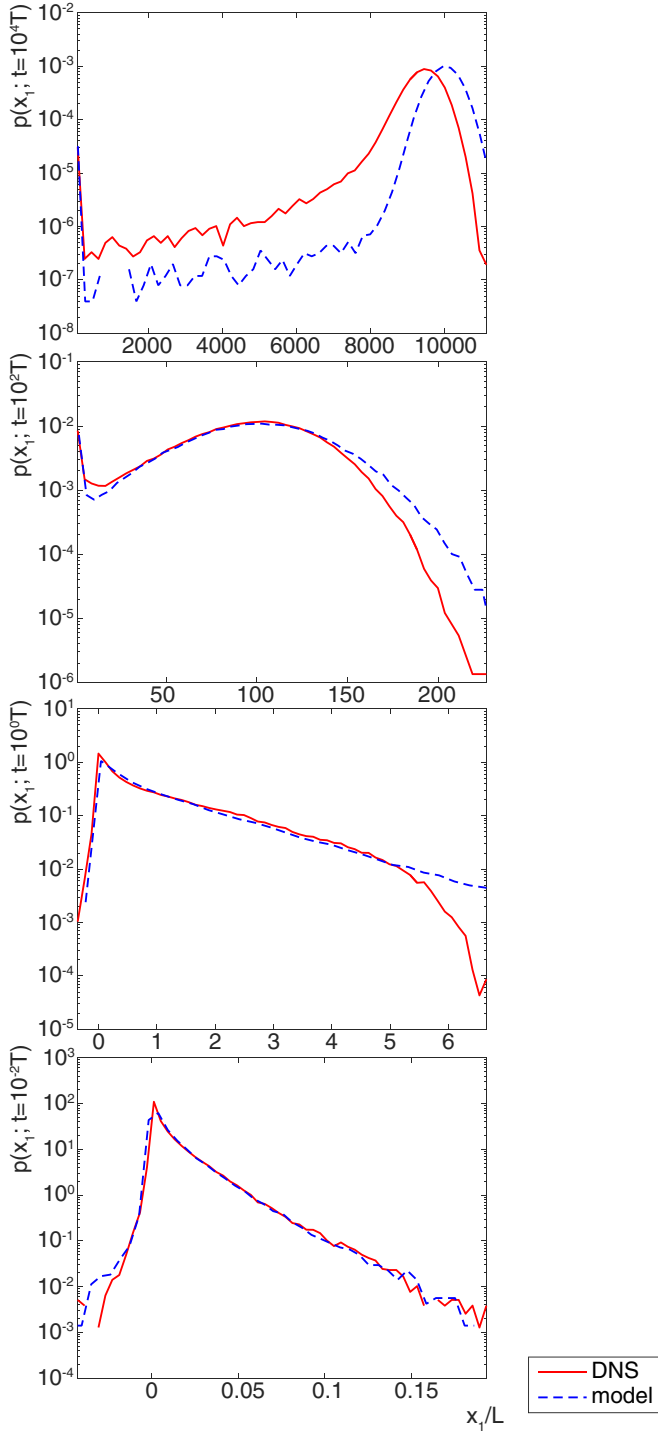


FIG. 4. See caption to Fig. 3. Data corresponding to the Ketton carbonate sample are depicted.

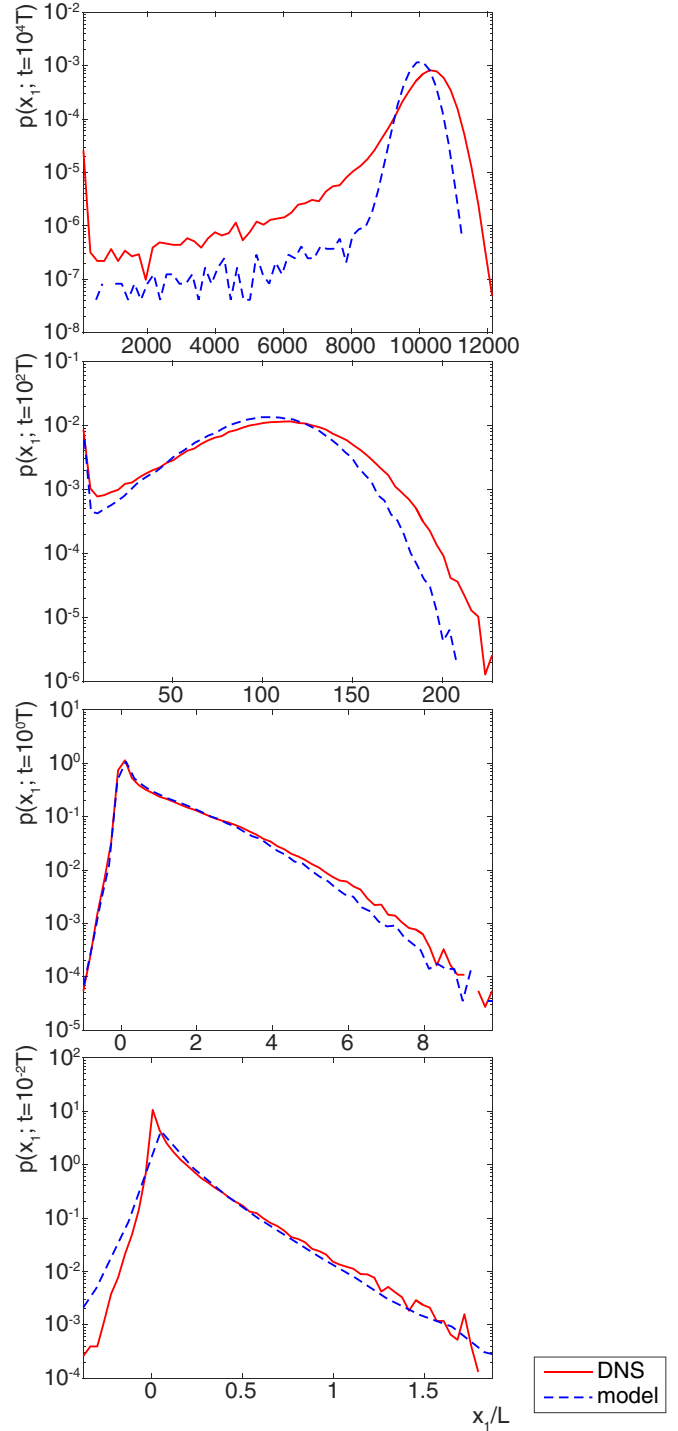


FIG. 5. See caption to Fig. 3. Data corresponding to the Bentheimer sandstone 1000 sample are depicted.

the logarithm, i.e., $v(t) \equiv \ln[u(t)/U]$. The PDF of the log velocity-magnitude $v(t)$ can then be parametrized to a good approximation for all samples with the skew-normal PDF,

$$p(v) = \frac{1}{\sqrt{2\pi}\sigma} \exp\left[-\frac{(v - \mu)^2}{2\sigma^2}\right] \operatorname{erfc}\left[-\frac{\alpha(v - \mu)}{\sqrt{2}\sigma}\right], \quad (1)$$

where μ , σ , and α are mean, standard deviation, and skewness parameters, respectively. These parameters reflect the

geometrical properties of flow paths in the porous medium. The temporal autocorrelation of $u(t)$, i.e., $\rho_u(t)$, shows for $t \geq 0$ a sharp and gradual decay in all samples. Plots of the velocity autocorrelation functions and log-velocity histograms are provided in Fig. 9. For Ketton and Bentheimer, $p(v)$ and $\rho_u(t)$ are almost equal, which explains the previously noted similarity in longitudinal spreading, since this process is governed essentially by $u(t)$. Together with the fact that the

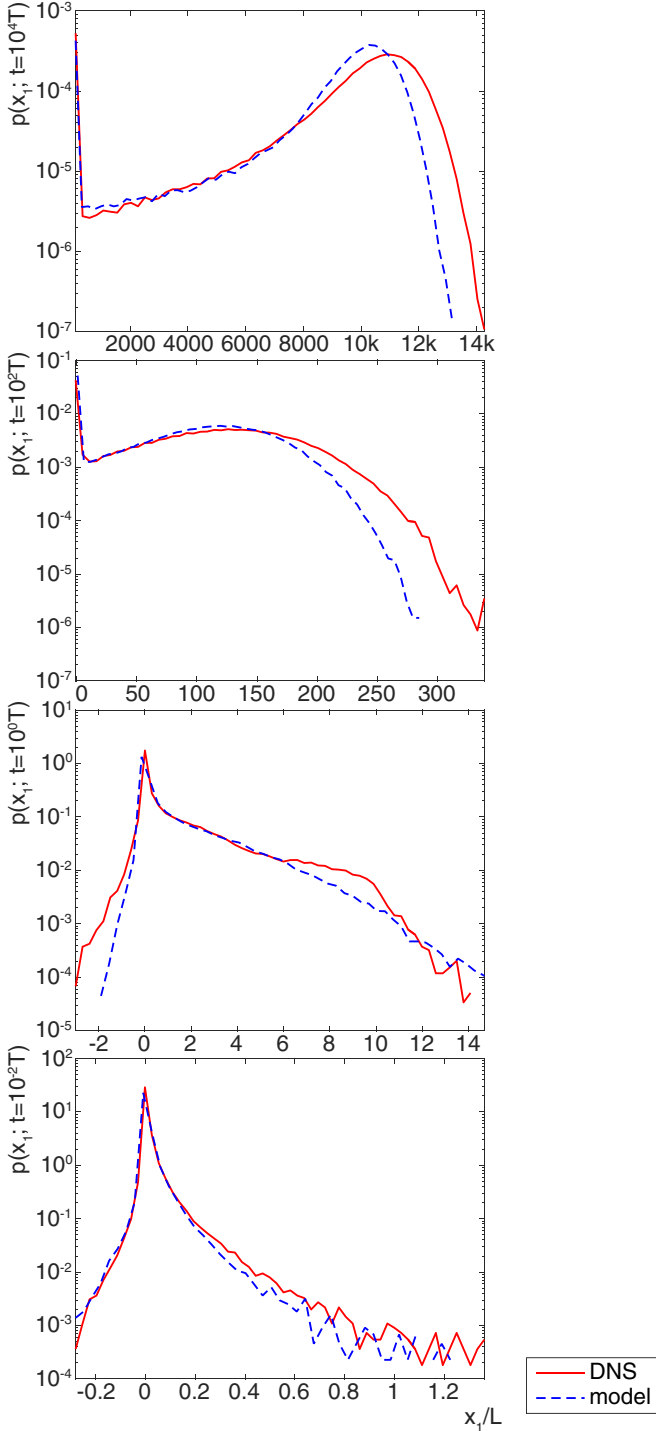


FIG. 6. See caption to Fig. 3. Data corresponding to the Estailades carbonate sample are depicted.

particle acceleration is approximately white-noise correlated, the sharp decay in $\rho_u(t)$ hints at a Markov model for $u(t)$. However to capitalize on our observation of skew-normality of $v(t)$, we formulated a Markov process for $v(t)$, i.e.,

$$dv = a(v)dt + \sqrt{d(v)}dW, \quad (2)$$

where dW is a random Wiener process increment and $a(v)$ and $d(v)$ are drift and diffusion functions, respectively [33].

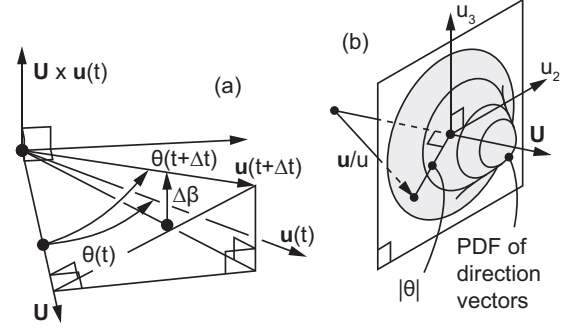


FIG. 7. (a) Local coordinate system spanned by the mean velocity $\mathbf{U} = (U, 0, 0)^T$ and the instantaneous particle velocity $\mathbf{u}(t)$. Positive angles are depicted. (b) Gaussian model for flow-direction vectors $\mathbf{u}(l)/u(l)$.

To determine the diffusion function $d(v) \equiv \lim_{\Delta t \rightarrow 0} \langle [v(t + \Delta t) - v(t)]^2 | v(t) = v \rangle / (\Delta t / T)$, we estimated the second transition moment of $v(t)$ based on our Lagrangian DNS data [34, Eqs. (3.85) and (4.44)]. For all samples, we found that $d(v)$ can be parametrized by the simple exponential model $d(v) = c \exp(bv)$. Here, the coefficient c quantifies the degree of fluctuation in $v(t)$, while b measures the growth of these fluctuations as v increases. Poorly connected samples like Estailades have flow fields with both stagnant zones and high-velocity flow paths (see Fig. 8). Accordingly, c is comparably large and since the flow path cross section shows typically high variability, b is large as well. For samples with a highly connected pore space such as bead packs, the flow fields show less variability and both c and b are smaller. With both the PDF of $v(t)$ and the diffusion function $d(v)$ parametrized, the drift function is determined by

$$p(v) = \frac{C}{d(v)} \exp \left[\int_{v_0}^v \frac{2a(v')}{d(v')} dv' \right], \quad (3)$$

which is the time-stationary solution of the Fokker-Planck equation that corresponds to Eq. (2) [33, Sec. 5.2.2]. This

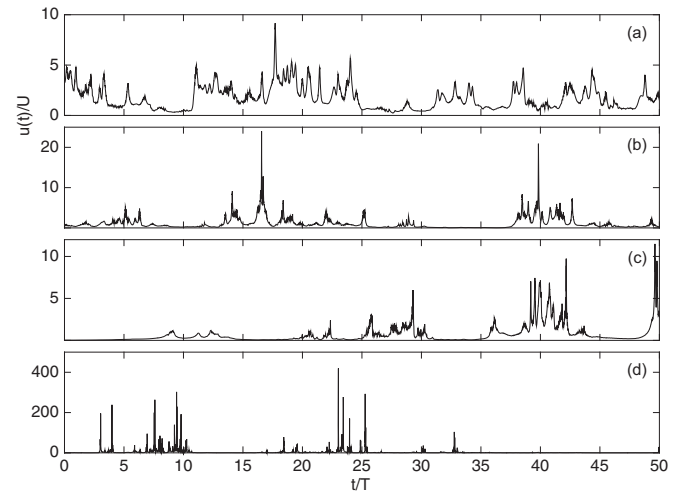


FIG. 8. Exemplary velocity-magnitude time series $u(t)$ resulting from randomly placed particles in different samples. (a) Bead pack 500, (b) Ketton, (c) Bentheimer 1000, (d) Estailades.

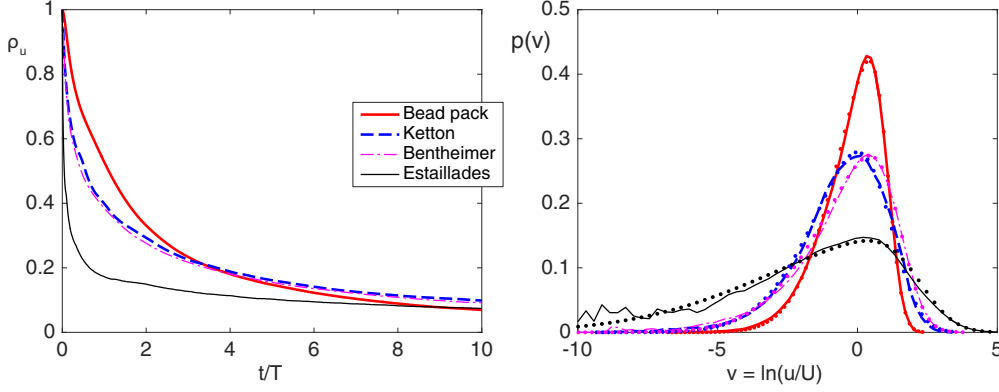


FIG. 9. Autocorrelation function $\rho_u(t)$ of the Lagrangian particle velocity $u(t)$ and histogram $p(v)$ of the log velocity-magnitude v . Dots represent the skew-normal model for $p(v)$.

expression with constants C and v_0 can be isolated for

$$a(v) = \frac{d(v)}{2} \frac{d}{dv} \ln[p(v)d(v)], \quad (4)$$

which fully determines the Markov model for the log velocity-magnitude process $v(t)$ and eventually $u(t)$ along a particle path line. An exemplary comparison of the parametric models of the drift and diffusion coefficients and their corresponding transition moment estimates is provided in Fig. 10. Function $a(v)$ results through Eq. (4) from the parametric models for $d(v)$ and PDF $p(v)$. Therefore, the agreement of $a(v)$ with the DNS transition moment data provides evidence in support of

our model formulation for $v(t)$. Moreover, one can observe that the exponential growth of $d(v)$ for increasing v is compensated in process Eq. (2) by an exponential decay of $a(v)$. The analytical link between $d(v)$, $a(v)$, and the stationary PDF $p(v)$ of process $v(t)$ is given by Eqs. (3) or (4).

B. Angle processes

The particle path-line geometry is determined from the angle processes $\theta(l)$ and $\beta(l)$. Since these processes are mainly influenced by the grain arrangement or pore-space geometry, we express them in terms of the travel distance $l(t) \equiv \int_0^t u(t')dt'$ [26]. If $\theta(l)$ and $\beta(l)$ are known, the entire path-line geometry can be assembled based on short path-line segments of length $\Delta l = u(t)\Delta t$. The segments are oriented as illustrated in Fig. 7(a) and determined by $\theta(l)$ and $\Delta\beta(l) = \beta(l + \Delta l) - \beta(l)$.

To arrive at a parametric model for the direction angle $\theta(l)$, we first consider the distribution of normalized flow-direction vectors $\mathbf{u}(l)/u(l)$ sampled equidistantly along particle path lines. As illustrated in Fig. 7(b), we assume that most vectors will be aligned with the mean flow. Accordingly, we use a bivariate Gaussian model for the PDF of the direction vectors [gray surface in u_2 - u_3 plane of Fig. 7(b)]. From this model we derived analytically the PDF

$$p(|\theta|) = \frac{|\theta|}{\sigma_\theta^2} \exp\left(-\frac{|\theta|^2}{2\sigma_\theta^2}\right), \quad (5)$$

with mean $\sqrt{\pi/2}\sigma_\theta$ for the absolute value of the direction angle $|\theta(l)|$. The variance parameter σ_θ^2 is directly related to the tortuosity since the latter can be expressed as

$$\begin{aligned} \kappa &= \frac{1}{\int_0^\infty \cos(|\theta|)p(|\theta|)d|\theta|} \\ &= \frac{1}{1 - \sqrt{2}\sigma_\theta \text{DawsonF}(\sigma_\theta/\sqrt{2})}, \end{aligned} \quad (6)$$

where the Dawson integral appears in the denominator. In support of the Gaussian assumption, we find good agreement of all angle PDFs extracted from our DNS data and our parametric model as is documented in Fig. 11.

The dynamics of $\theta(l)$ are much more complex than in our earlier work [26] with the autocorrelation function $\rho_\theta(l)$ having

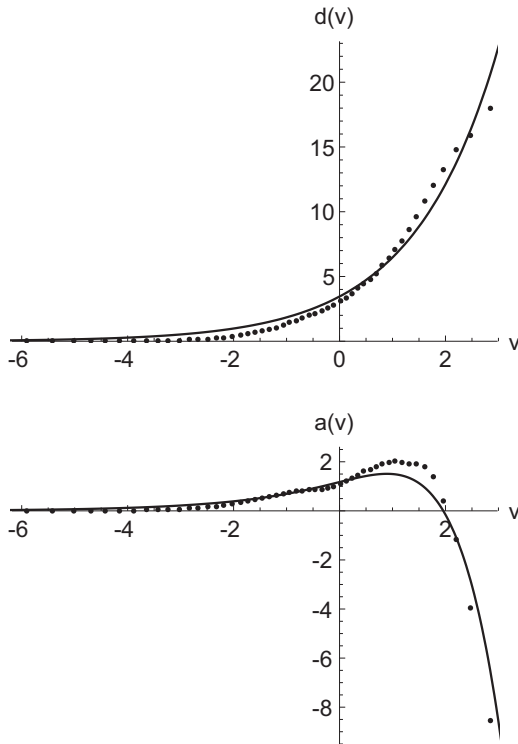


FIG. 10. Drift and diffusion coefficients $a(v)$ and $d(v)$, respectively, for the log velocity-magnitude process $v(t)$ of the Estailades carbonate sample. Depicted are the parametric fits (lines) and the transition moments (dots).

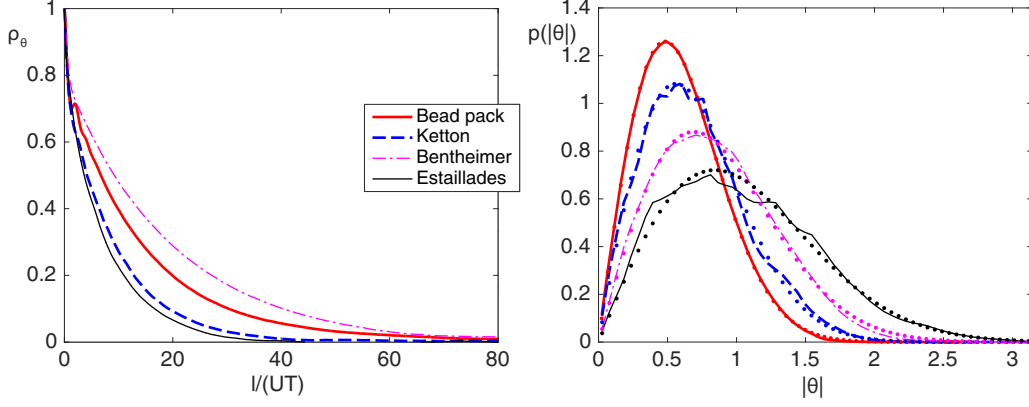


FIG. 11. Autocorrelation function $\rho_\theta(l)$ of the Lagrangian velocity direction-angle $\theta(l)$ and histogram $p(|\theta|)$. Dots represent the analytical model given by Eq. (5) for $p(|\theta|)$.

a sharp drop at $l \approx 0$ followed by a gradual decay to zero. This behavior is shown in Fig. 11 and is resulting from the combined effect of regular oscillations and occasional abrupt sign changes in θ . To model this behavior accurately, we treat the two effects with two designated random processes. An analysis of the autocorrelation of $|\theta(l)|$ (not shown) reveals an oscillatory behavior for the bead packs and Ketton sample that is resulting from the spherical grains. For Bentheimer and Estailades the autocorrelation of $|\theta(l)|$ decays monotonically to zero within four $l/(UL)$. To model these dynamics, we apply the integral process $z_\theta(l)$ of a noisy harmonic oscillator $y_\theta(l)$ [34, Sec. 10.2], i.e.,

$$dz_\theta = y_\theta dl, \quad \text{with} \\ dy_\theta = -\left(\omega_{\theta\theta}^2 z_\theta + \frac{y_\theta}{\tau_\theta}\right) dl + b_\theta \sqrt{\frac{2}{\tau_\theta}} dW. \quad (7)$$

Process $z_\theta(l)$ has a Gaussian stationary PDF and to recover the PDF of $|\theta(l)|$ given by Eq. (5) the analytically derived mapping,

$$|\theta| = \sigma_\theta \sqrt{\ln(4) - 2 \ln[\text{erfc}(\omega_\theta z_\theta / \sqrt{2})]}, \quad (8)$$

is applied including the complementary error function erfc . Inspection of the Lagrangian DNS data depicted in Fig. 12

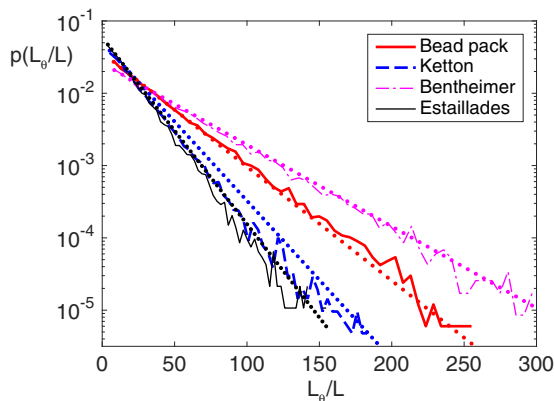


FIG. 12. Histogram of the travel-distance L_θ with no sign change in $\theta(l)$. Dots represent the exponential PDF model.

reveals that the lengths L_θ of periods with equal sign in $\theta(l)$ are distributed by the exponential PDF $p(L_\theta/L) = \exp[-(L_\theta/L)/\mu_\theta]/\mu_\theta$ for all media considered. By combining all listed elements, we found that a description for $\theta(l)$ based on Eq. (8) for $|\theta(l)|$ and the exponentially distributed travel-distance L_θ for the sign of $\theta(l)$ can very accurately reproduce $\rho_\theta(l)$ for all samples.

By analyzing the compensated variance evolution $\langle [\beta(l+s) - \beta(l)]^2 \rangle / s$ in the semilogarithmic plot (see Fig. 13), we consistently observe for all samples a transition from zero to a higher plateau at large s . This is characteristic of an integrated Ornstein-Uhlenbeck process [34, Sec. 3.1], which we applied to model $\beta(l)$, i.e.,

$$d\beta = y_\beta dl, \quad \text{with} \quad dy_\beta = -\frac{y_\beta}{\tau_\beta} dl + b_\beta \sqrt{\frac{2}{\tau_\beta}} dW. \quad (9)$$

C. Summary and validation

In summary, our stochastic model is composed of a Lagrangian log velocity-magnitude process $v(t)$ in time t with exponential diffusion coefficient and stationary PDF parametrized by b, c and α, μ, σ , respectively. The spatial velocity direction is determined by two direction angles $\theta(l)$ and

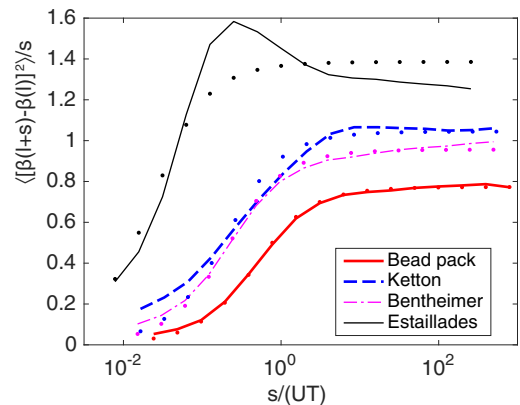


FIG. 13. Compensated variance evolution $\langle [\beta(l+s) - \beta(l)]^2 \rangle / s$ as a function of separation distance s . Dots represent the compensated variance resulting from the integrated Wiener process model.

$\beta(l)$ as a function of travel distance l . The θ process involves a standard deviation parameter σ_θ , a noisy harmonic oscillator with parameters $\omega_{0\theta}$ and τ_θ , and a sign process with parameter μ_θ . The β process is based on an Ornstein-Uhlenbeck process with parameters τ_β and b_β . The process parameters for the different samples are summarized in Fig. 14. Each column represents a parameter set of a specific sample that may be interpreted as a transport “fingerprint” of each sample. One can observe that fingerprints of samples from the same rock type but different sample sizes are similar. Moreover, while parameter sets of Ketton carbonate and Bentheimer sandstone are similar, the bead pack and Estailades sets are significantly different.

Particle path lines that resulted from the previously outlined model and listed parameters are compared with their DNS counterparts in Fig. 15. The path line characteristics of the selected media show strong differences, which is represented well by the statistical model. A qualitative comparison between the DNS reference and our statistical model is provided in Fig. 2. The model reproduces the longitudinal spreading behavior accurately but shows deviations in transverse direction. The transverse asymptotic behavior, however, is captured correctly. In Figs. 3–6, detailed comparisons of the plumes in x_1 direction for all media including the most complex medium, i.e., Estailades, are provided. While in Ref. [19] detailed model comparisons were reported for Berea sandstone up to 10 nondimensional time units, we validate our model for four different media up to $t/T = 10^4$ and obtain results of

angle $\theta(l)$	$\omega_{0\theta}$	3.6	3.6	5.1	5.0	4.3	10
	τ_θ	0.28	0.3	0.11	0.093	0.12	0.018
	σ_θ	0.48	0.48	0.56	0.59	0.69	0.84
angle $\beta(l)$	μ_θ	26	28	20	41	38	17
	τ_β	0.22	0.29	0.12	0.11	0.13	0.014
log velocity-magnitude $v(t)$	b_β	1.3	1.1	2	2	1.9	7
	b	0.26	0.25	0.53	0.56	0.57	0.63
	c	0.7	0.65	0.87	1.1	1.3	3
	α	-3.8	-4	-2.6	-4.7	-3.6	-5.1
	μ	1.1	1.1	1.1	1.5	1.5	2.2
σ	1.6	1.7	2.3	2.7	2.5	5.1	
		Bead 300	Bead 500	Kett.	Bent. 300	Bent. 1000	Estailades

FIG. 14. List of parameters of our stochastic transport model. The rows correspond to different parameters and the columns to different samples. The gray level encodes the parameter value.

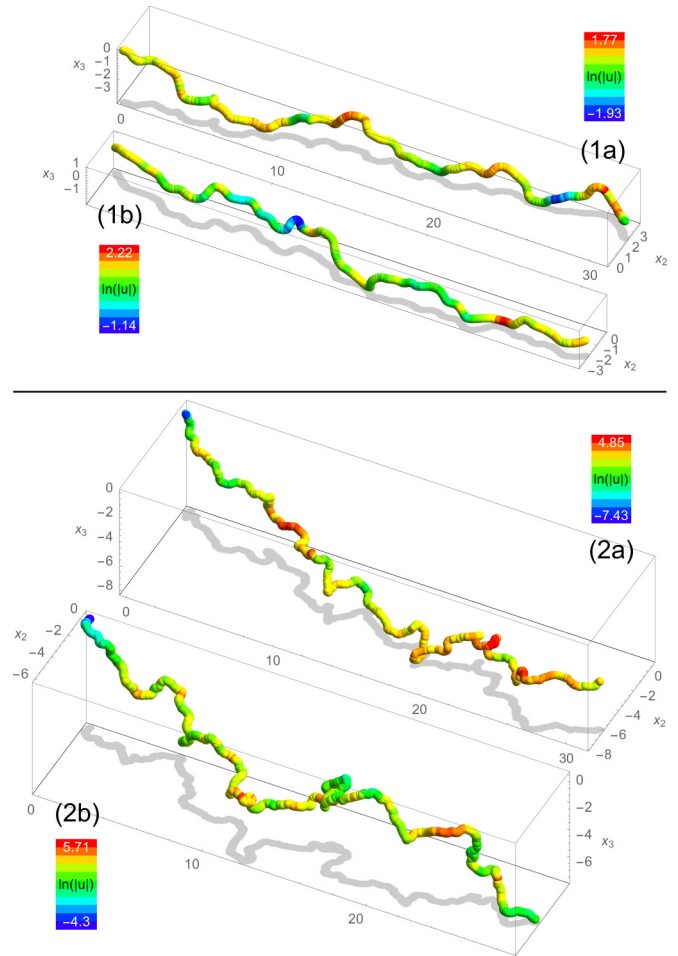


FIG. 15. Exemplary particle path lines tracked in the (1) monodisperse bead pack and (2) Estailades carbonate. Panels correspond to path lines from (a) DNS and (b) the statistical model. The color represents $\ln[u(t)/U]$.

very similar accuracy. We point out the good performance of the model for the comparably complex carbonates.

IV. CONCLUSIONS

In summary, we presented a framework that relates the microscopic pore structure to the emerging macroscopic dispersion behavior. To this end, a universal statistical transport model that employs a spatiotemporal Markov process was devised whose parametrization is based on the geometrical properties of flow paths. While longitudinal dispersion was found to depend on the connectivity or roughness of these flow paths, transverse dispersion depends on their tortuosity. The dispersion predictions that resulted from our model were found to be valid for a range of porous media, including highly complex carbonates.

In the case with molecular diffusion added, the particle motion is a combination of thermal Brownian motion and advective transport [35] and the velocity dynamics are expected to become less complex. This is because molecular diffusion will enhance the mobilization of trapped particles in stagnant flow regions, which will simplify the temporal

correlation behavior of $u(t)$ and enhance Fickian dispersion. More specifically, the peaks representing trapped particles in the particle plumes will diffuse more quickly [18, Figs. 12 and 13]. Molecular diffusion effects become appreciable below Péclet numbers between 300 and 600 depending on the media [36, Eq. (11.48)], [16].

To resolve the deviations in transverse direction, a more detailed analysis of the angle processes is necessary. Finally, except for the bead pack, larger samples are needed to avoid boundary effects in transverse direction and to have more statistical variability of the pore-space geometry. This last point is most critical in the Estailades sample, where the velocity correlation length λ is approximately three times the sample size L_0 . The acquisition and processing of larger-sized

samples will be the subject of further development in the experimental techniques and computational capabilities. As an alternative to the acquisition of large samples, we consider the use of artificially generated samples, e.g., by means of the recently outlined cross-correlation method [37].

Data sets used in this work are available online [38].

ACKNOWLEDGMENTS

The authors acknowledge helpful discussions with Patrick Jenny and Martin J. Blunt and helpful comments of the anonymous reviewers. Moreover, Daniel Meyer acknowledges funding by ETH Zürich and is grateful to Sam Hollman for his help during the preparation of this manuscript.

-
- [1] C. F. Harvey, *Nature* **454**, 415 (2008).
 - [2] G. Hirasaki, C. A. Miller, and M. Puerto, *SPE J.* **16**, 889 (2011).
 - [3] D. P. Schrag, *Science* **325**, 1658 (2009).
 - [4] M. Sahimi, *Rev. Mod. Phys.* **65**, 1393 (1993).
 - [5] U. M. Scheven, D. Verganelakis, R. Harris, M. L. Johns, and L. F. Gladden, *Phys. Fluids* **17**, 117107 (2005).
 - [6] M. Moroni and J. H. Cushman, *Water Resour. Res.* **37**, 873 (2001).
 - [7] M. Moroni, J. H. Cushman, and A. Cenedese, *Int. J. Eng. Sci.* **41**, 337 (2003).
 - [8] D. Sen, D. Nobes, and S. Mitra, *Microfluidics and Nanofluidics* **12**, 189 (2012).
 - [9] S. S. Datta, H. Chiang, T. S. Ramakrishnan, and D. A. Weitz, *Phys. Rev. Lett.* **111**, 064501 (2013).
 - [10] A. Scheidegger, *J. Geophys. Res.* **66**, 3273 (1961).
 - [11] J. Bear, *Dynamics of Fluids in Porous Media* (American Elsevier, New York, 1972), p. 764.
 - [12] S. Torquato, *Random Heterogeneous Materials Microstructure and Macroscopic Properties*, 2nd ed., Interdisciplinary Applied Mathematics (Springer, New York, 2006), p. 701.
 - [13] S. Peng, F. Marone, and S. Dultz, *J. Hydrol.* **510**, 403 (2014).
 - [14] N. H. Pham, R. S. Voronov, N. R. Tummala, and D. V. Papavassiliou, *Phys. Rev. E* **89**, 033016 (2014).
 - [15] A. T. Borujeni, N. M. Lane, K. Thompson, and M. Tyagi, *Comput. Fluids* **88**, 753 (2013).
 - [16] B. Bijeljic, P. Mostaghimi, and M. J. Blunt, *Phys. Rev. Lett.* **107**, 204502 (2011).
 - [17] B. Bijeljic, A. Raeini, P. Mostaghimi, and M. J. Blunt, *Phys. Rev. E* **87**, 013011 (2013).
 - [18] B. Bijeljic, P. Mostaghimi, and M. J. Blunt, *Water Resour. Res.* **49**, 2714 (2013).
 - [19] P. K. Kang, P. de Anna, J. P. Nunes, B. Bijeljic, M. J. Blunt, and R. Juanes, *Geophys. Res. Lett.* **41**, 6184 (2014).
 - [20] G. M. Porta, B. Bijeljic, M. J. Blunt, and A. Guadagnini, *Geophys. Res. Lett.* **42**, 7537 (2015).
 - [21] M. Rolle, D. Hochstetler, G. Chiogna, P. Kitanidis, and P. Grathwohl, *Transp. Porous Media* **93**, 347 (2012).
 - [22] R. C. Acharya, A. J. Valocchi, C. J. Werth, and T. W. Willingham, *Water Resour. Res.* **43**, W10435 (2007).
 - [23] O. A. Cirpka, E. O. Frind, and R. Helmig, *J. Contam. Hydrol.* **40**, 159 (1999).
 - [24] P. de Anna, T. Le Borgne, M. Dentz, A. M. Tartakovsky, D. Bolster, and P. Davy, *Phys. Rev. Lett.* **110**, 184502 (2013).
 - [25] T. Le Borgne, M. Dentz, and J. Carrera, *Phys. Rev. E* **78**, 026308 (2008).
 - [26] D. W. Meyer, H. A. Tchelepi, and P. Jenny, *Water Resour. Res.* **49**, 2359 (2013).
 - [27] D. W. Meyer and H. A. Tchelepi, *Water Resour. Res.* **46**, W11552 (2010).
 - [28] C. M. Sayers, *Leading Edge* **27**, 1020 (2008).
 - [29] J. L. Finney, *Proc. R. Soc. London A* **319**, 479 (1970).
 - [30] M. Prodanovic and S. L. Bryant, *J. Colloid Interface Sci.* **304**, 442 (2006).
 - [31] P. Mostaghimi, B. Bijeljic, and M. Blunt, *SPE J.* **17**, 1131 (2012).
 - [32] D. W. Pollock, *Ground Water* **26**, 743 (1988).
 - [33] C. W. Gardiner, *Handbook of Stochastic Methods for Physics, Chemistry, and the Natural Sciences*, 3rd ed. (Springer, Berlin, 2004), p. 415.
 - [34] H. Risken, *The Fokker-Planck Equation: Methods of Solution and Applications*, 2nd ed. (Springer, Berlin, 1989), p. 472.
 - [35] B. P. van Milligen and P. D. Bons, *Phys. Rev. E* **85**, 011306 (2012).
 - [36] M. Sahimi, *Flow and Transport in Porous Media and Fractured Rock: From Classical Methods to Modern Approaches* (VCH, Weinheim/New York, 1995), pp. xiv, 482 p.
 - [37] P. Tahmasebi and M. Sahimi, *Phys. Rev. Lett.* **110**, 078002 (2013).
 - [38] <http://www.digitalrocksportal.org>.